

## Chapter

# Shrinkage Porosity in Steel Sand Castings: Formation, Classification and Inspection

*Nawaz Mahomed*

## Abstract

In this Chapter, shrinkage porosity defects in steel castings are analysed, particularly for low carbon, high alloyed steels, which have applications in critical engineering components. It begins with the mechanisms for porosity formation within the solidification contraction phase of the casting cycle, highlighting the importance of feeder design. This is followed by characterisation of the solidification phase of steel alloys, including the evolution of phases, which is important in distinguishing between microstructure and porosity in microscopy analysis. A more detailed discussion of interdendritic feeding and mechanisms for shrinkage micro-porosity is then provided. This leads to the well-established interdendritic flow model and commonly-used thermal criteria for shrinkage porosity prediction. The discussions are then consolidated through the classification of shrinkage porosity in terms of formation mechanisms and morphology, and its causes relating to composition, design and process conditions. Finally, engineering standards for classification and inspection of porosity types and severity levels in steel castings are discussed. Throughout, basic design and process improvement approaches for improving melt feeding during solidification contraction is given, with emphasis on providing practical solutions for prediction and evaluation of shrinkage porosity defects in castings.

**Keywords:** Shrinkage porosity, solidification, peritectic steels, digital radiography inspection

## 1. Introduction

Steel castings used in high-performance applications, such as cast valve components used in power plants and automotive engines, are subject to stringent quality standards to ensure operational integrity. Such steels may vary from high carbon low alloy steels to low carbon high alloyed steels, the latter designed to withstand highly-corrosive environments and have low susceptibility to brittle fracture. Metal castings of all material and process types are prone to porosity, defined as internal voids or non-metallic inclusions, and classified as internal defects (similar to other internal defects, such as the evolution of unwanted material phases or inhomogeneities in the distribution of alloying elements due to segregation phenomena). Such porosity defects can severely impact the performance of castings, through crack initiation and propagation under fatigue loading, stress corrosion cracking, and

reduced material strength and (hence) fatigue life, among other factors [1–3]. It is therefore common that allowable limits on porosity severity levels are dictated by standards or client specifications. At the same time, it is therefore crucial that foundries develop a clear understanding of porosity defects in (steel) castings and introduce suitable monitoring and improvement protocols in order to remain competitive.

Porosity can generally be categorised as gas porosity (entrapped and segregated gases), inclusions (sand and slag), shrinkage porosity, and hot tears (also known as hot cracks) [4]. Furthermore, these different types of porosity may present both at the micro and macro length scales. These porosity types and their length scales, together with their morphologies, provide clues as to their likely causes, allowing the introduction of mitigation measures by foundries.

This Chapter focuses on shrinkage porosity in steel sand castings. Sandcasting, in particular, is a process that depends on gravitationally pressurised flow, which makes it difficult to feed the solidification contraction of the metal. This makes sandcast components, which is the case for most steel components, prone to shrinkage porosity. In some cases, geometric modifications to part geometry can eliminate shrinkage porosity. However, in other cases, it is unavoidable, but can be reduced through a combination of geometric and process modifications.

During the casting cycle, the steel undergoes three types of contractions that need to be considered, as illustrated in **Figure 1**.

- Firstly, the thermal contraction in the liquid state. In some practices, the liquid melt pouring temperature  $T_p$  is kept higher to avoid early formation of skin freezing, allowing the metal to solidify directionally inward from the surface. However, it is important to establish whether higher pouring temperatures lead to higher or lower shrinkage porosity. In any case, liquid melt contraction is not an issue in foundries, since its low value ( $< 1\%$ ) is easily compensated through liquid feeding from the feeders. The liquid melt density as a function of temperature  $T$  [K] and carbon content  $C$  [%wt] can be determined using the empirical relationship [5]:

$$\rho = (7.10 - 0.0732C) - (8.28 - 0.874C) \times 10^{-4}(T - 1823) \quad (1)$$

and the density of solid steel can be determined using Thermo-Calc or similar computational thermodynamic systems.

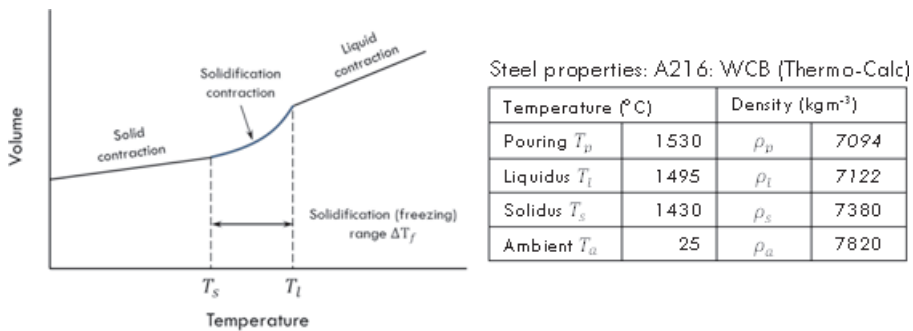


**Figure 1.** Contraction of steel during a casting cycle for a low carbon steel (A216 WCB with  $C = 0.3\%$ ,  $T_{liquidus} = 1495^\circ\text{C}$ ,  $T_{solidus} = 1430^\circ\text{C}$ ): liquid contraction = 0.4%; solidification contraction = 3.6%; solid contraction = 6.0% (Data from Thermo-Calc and [5]).

- Secondly, the contraction during solidification in the mushy state, when the liquid metal transforms to the initial solid state microstructure. Contractions for some pure metals at their respective freezing temperatures are given in [4]. In the case of pure Fe, the solidification contraction was found to be 3.16% at the phase transformation temperature of 1536°C. However, as the carbon content increases, it increases to up to 5% for low carbon steels. This is related to the decrease in the solidus temperature as the carbon content increases (see phase diagram in **Figure 2**). The importance of solidification contraction is two-fold: (i) the need for an efficient feeder system to compensate for solidification contraction, and (ii) the formation of shrinkage porosity as a result of failure to feed the mushy zone – this is unavoidable due to coherency of the dendritic structure when the mushy zone reaches a particular solid fraction, leading to entrapped interdendritic liquid

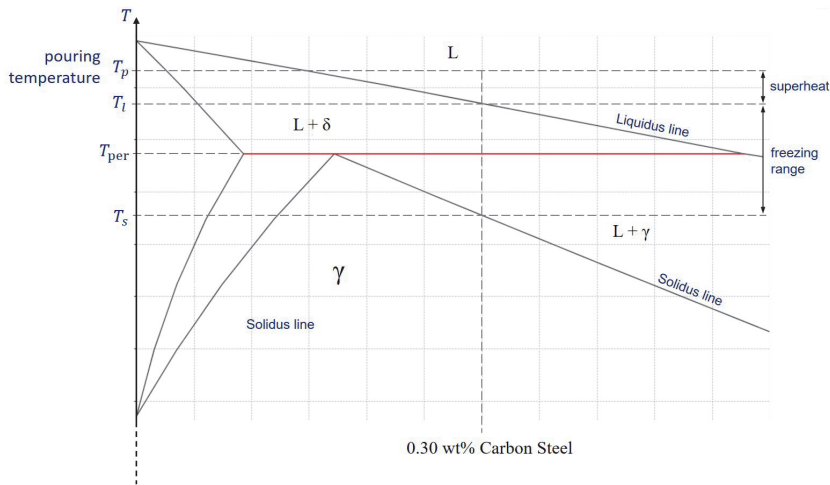


**Figure 2.**  
 Temperature profile during the solidification stage of a typical low carbon steel.

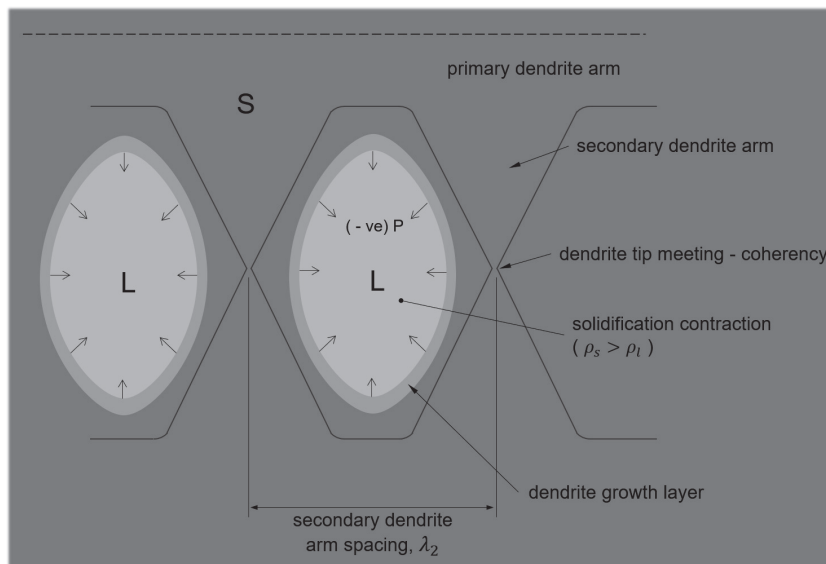


**Figure 3.**  
 Mushy zone coherency during solidification shrinkage.

melt, which results in either pore nucleation (due to volumetric shrinkage) or solid collapse (due to negative pressure), as shown in **Figure 3**. As will be shown later, the freezing range (difference between the liquidus and solidus temperatures) is an important factor in determining the morphology of shrinkage pores.

- Thirdly, the solid state contraction of the metal. Even though solid-state solidification values may be used in foundries (especially for pattern design), metals are rarely free to contract due to various microstructural constraints – this leads to internal stresses, and where these stresses overcome resistance, the material can undergo plastic or viscoplastic strain to adapt to the thermal and transformational density changes. Hence, the part may be larger than predicted. These constraints can lead to localised cold cracking (initiated from hot tears during solidification contraction).

## 2. Feeder System Design for Solidification Contraction

Attention is focused on the second stage, i.e. solidification contraction in the mushy zone, which is the root cause of shrinkage porosity. Initially, as stated above, a feeder system is required to compensate for solidification contraction, but also to ensure that shrinkage porosity formation is minimised. This requires that the feeder/s (a) must contain sufficient melt volume to compensate for the volume contraction of the part, and, more importantly, (b) solidify later than the casting (see **Figure 4**). The latter effectively implies that the thermal centre of the total casting should eventually migrate to the feeder/s, where high porosity formation due to hotspots or in the form of pipe shrinkage will be experienced.

Applying the two requirements for feeder design, firstly, the volume of the feeder/s is given by:

$$V_f \approx \alpha V_c$$

where  $\alpha$  = shrinkage fraction,  $V_f$  = feeder/s volume and  $V_c$  = cavity volume. Taking account of shrinkage within the feeder itself:

$$V_f - \alpha V_f = \alpha V_c$$

However, feeders in sandcasting moulds have low levels of feeding efficiency due to gravitational feeding and low design heads, giving:

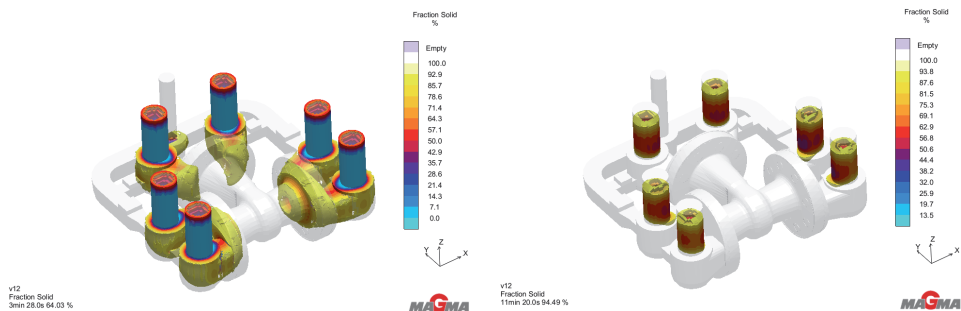


**Figure 4.** Solid fraction predictions for a valve body casting at two different times, showing the feeders (with exothermic sleeves) solidifying later than the casting.

$$eV_f = \alpha(V_c + V_f) \quad (2)$$

where the feeder efficiency  $e$  is generally taken to be in the range of 15–30%. It is necessary to balance the feeder efficiency with feeder size to avoid high waste and energy consumption. Secondly, the solidification time of the feeder/s must be greater than that of the casting, typically by a “safety factor” of 1.2, giving:

$$t_s|_{casting} < t_s|_{feeder} \implies t_s|_{feeder} = 1.2t_s|_{casting} \quad (3)$$

The well-known Chvorinov’s equation allows the above relation to be expressed in terms of the mould geometry, and can be expressed as:

$$t_s = B \left( \frac{V}{A} \right)^n \quad (4)$$

where  $V$  is the casting volume,  $A$  is the surface area of the casting through which heat is conducted,  $n$  is an empirical exponent (equal to 2 for simply shaped castings in silica sand moulds), and  $B$  is the moulding constant which is dependent on (a) process parameters (the equilibrium solidification temperature  $T_m$ , the initial temperature  $T_0$  of the mould, and the superheat  $\Delta T_s = T_{pour} - T_m$ , all in °K), (b) mould material properties (thermal conductivity  $k$  in  $W \cdot m^{-1} \cdot K^{-1}$ , density  $\rho$  in  $kg \cdot m^{-3}$ , and specific heat capacity  $c$  in  $J \cdot kg^{-1} \cdot K^{-1}$ ), and (c) casting metal properties (latent heat of fusion  $L$  in  $J \cdot kg^{-1}$ , density  $\rho_m$  in  $kg \cdot m^{-3}$ , and specific heat capacity  $c_m$  in  $J \cdot kg^{-1} \cdot K^{-1}$ ), given by:

$$B = \left[ \frac{\rho_m L}{T_m - T_0} \right]^2 \left[ \frac{\pi}{4k\rho c} \right] \left[ 1 + \left( \frac{c_m \Delta T_s}{L} \right)^2 \right] \quad (5)$$

Although Eq. (4) may appear complex, it is relatively straightforward to evaluate given the casting process parameters deployed and the materials used for the sandmould and the casting, the latter being readily available in metal casting databases. It is therefore relatively easy to estimate the solidification time for a specific cast geometry. However, in the design of the feeder system, this is not necessary, since substituting Eq. (3) into Eq. (2) simply requires that:

$$\frac{V_f}{A_f} = 1.2 \frac{V_c}{A_c} \implies m_f = 1.2m_c \quad (6)$$

where the modulus  $m$  has been introduced. Solving Eqs. (1) and (5) simultaneously for a given mould cavity allows the dimensioning of the system of feeders.

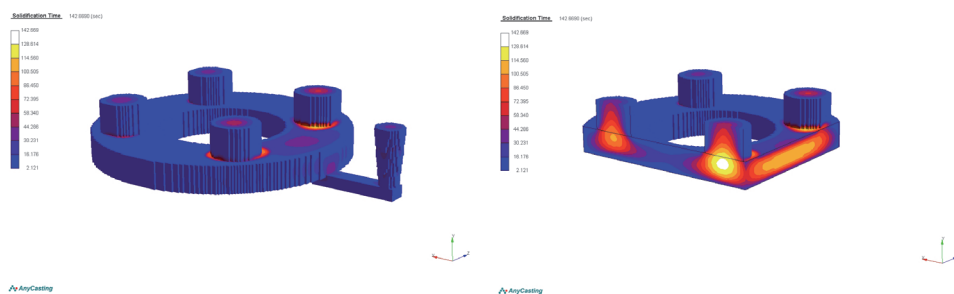


**Figure 5.**  
 Hotspot formation in the feeder junction regions and the gate area of a steel disc casting for a modulus  $m_f/m_c = 1.2$ .

The effect of the modulus ratio  $m_f/m_c$  on shrinkage porosity is quite significant – with no feeding (i.e. modulus ratio = 0), shrinkage porosity as high as 7% can result. However, whilst modulus ratios higher than 1.2 can significantly reduce shrinkage porosity, it will not be entirely eliminated due to interdendritic phenomena. That is, the inclusion of oversized feeders does not guarantee sufficient pressure differentials to feed the solidifying dendritic network. This will be the subject of further investigation in the next section.

Furthermore, the modulus ratio of 1.2 does not guarantee the formation of hotspots in the junction region between the part and the feeder, as shown in **Figure 5**. This can be resolved through increasing the modulus ratio, albeit at the cost of production. However, a better approach would be to use exothermic sleeves around the feeders, as can be seen in **Figure 4**.

### 3. Interdendritic feeding

#### 3.1 Solidification Characterisation of Steels

Before analysing interdendritic feeding, it is important to establish some important casting-related parameters of the steel during the solidification stage. These include the liquidus and solidus temperatures for the particular steel grade, so as to ascertain the superheat during pouring (i.e. the temperature difference between the pouring temperature ( $T_p$ ) and the onset of solidification at the liquidus temperature ( $T_l$ )), and the freezing range (difference between the liquidus temperature ( $T_l$ ) and solidus temperature ( $T_s$ )). In addition, the partition coefficient ( $k$ ) and liquidus slope ( $m$ ) are related to the evaluation of shrinkage porosity, as will be seen later.

Steels are generally alloyed, as well as post-cast heat-treated, to produce a desired microstructure (and hence specifically desired properties). Although the alloying levels (of chromium, nickel, etc.) may range from low (plain carbon steels) to high (stainless steels), the carbon composition plays a dominant role in determining dendrite size (and hence shrinkage porosity) of the solidifying melt [6, 7]. Of particular interest are low carbon steels, with carbon content in the range up to 0.3% wt. Such steels undergo a peritectic transformation during solidification at the peritectic temperature ( $T_{per}$ ), at which  $\delta$ -ferrite and liquid transforms into austenite. A number of empirical models can simply be used for determining the aforementioned temperatures for multi-component steels [8]. In this analysis, the binary (Fe-C) phase diagram of steel with C = 0.3%, as shown in **Table 1**, will be used to demonstrate these temperatures and their effect on shrinkage porosity<sup>1</sup>.

The Fe-C phase diagram shown in **Figure 7** was generated using Thermo-Calc. For a steel with C = 0.3%wt, solidification starts at the liquidus temperature  $T_l = 1515^\circ\text{C}$  with the nucleation of BCC  $\delta$ -ferrite, and proceeds until the peritectic temperature,  $T_{per} = 1495^\circ\text{C}$  is reached. This is referred to as the  $L + \delta$  zone.

At this point, for the hyperperitectic (above C = 0.17%) steel, the phase fractions of value of  $\delta$ -ferrite (of 0.10%C) can be calculated using the lever rule as follows:

$$\delta\text{-ferrite} : g_\delta = \frac{0.53 - 0.30}{0.53 - 0.10} = 0.53 \quad \text{and} \quad \text{liquid} : g_l^{per} = 1 - g_\delta^{per} = 0.47$$

<sup>1</sup> For an actual steel grade, the phase diagram will be slightly different due to the influence of the alloying elements. See **Figure 6** for the case of A216 WCB steel, showing an additional  $L + \delta + \gamma$ .

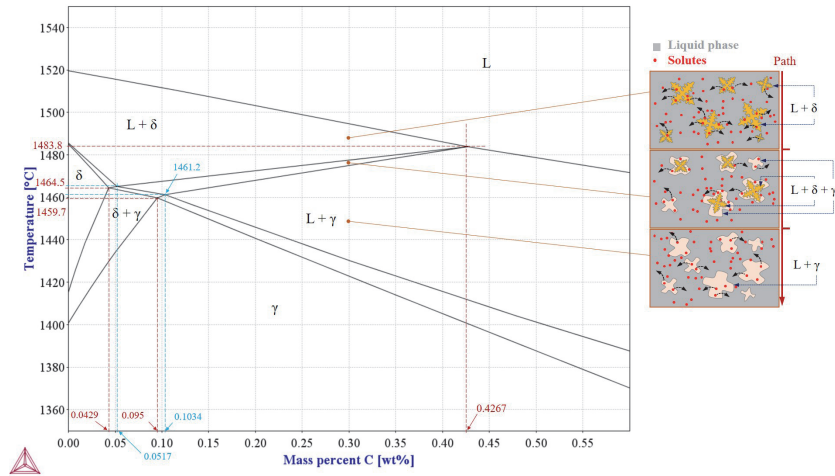


**Figure 6.** Phase transformation of A216 WCB steel in the peritectic region (solidification zones), showing nucleation and growth of  $\delta$ -ferrite and austenite at the respective transition zones across the freezing range from  $T_l = 1495^\circ\text{C}$  to  $T_s = 1430^\circ\text{C}$  (freezing range =  $65^\circ\text{C}$ ), as well as solute rejection.

C	Mn	P	S	Si	Cu	Ni	Cr	Mo	V
As per ASTM A216 Material Standard									
0.30	1.00	0.035	0.035	0.6	0.30	0.50	0.50	0.20	0.03

**Table 1.** Chemical composition (% wt) of A216 WCB cast steel.

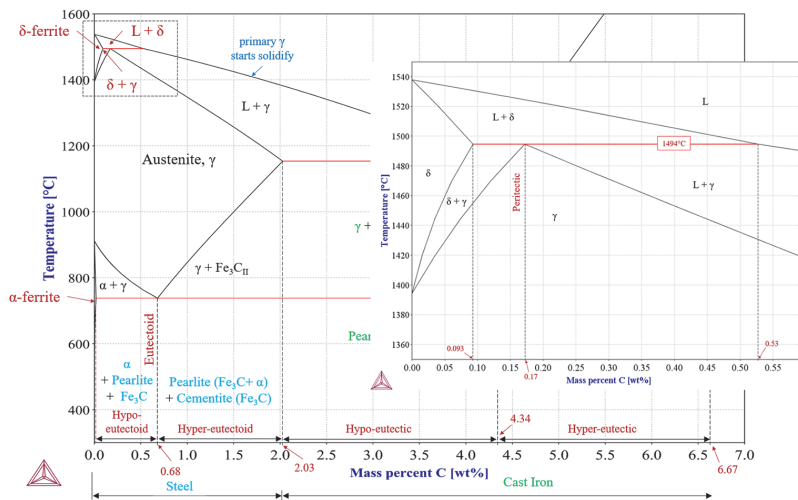


**Figure 7.** Phase diagram of Fe-C cast steel, showing the peritectic region enlarged (generated using Thermo-Calc).

Now, for peritectic transformation to occur, using the lever rule at  $C = 0.17\%$  (peritectic composition), the fractions of  $\delta$ -ferrite (of  $0.10\%$  C) and liquid (of  $0.53\%$  C) are given as:

$$\delta - \text{ferrite} : g_{\delta}^{\text{per}} = \frac{0.53 - 0.17}{0.53 - 0.10} = 0.84 \quad \text{and} \quad \text{liquid} : g_l^{\text{per}} = 1 - g_{\delta}^{\text{per}} = 0.16$$

Hence, in our case of a hyperperitectic steel ( $C = 0.3\%$ ), there is a shortage of  $\delta$ -ferrite to react with the amount of liquid fraction for a full peritectic transformation to austenite. The amount of liquid fraction that is transformed with the  $\delta$ -ferrite fraction of 0.53 into austenite at the peritectic temperature is only  $0.53/0.84 \times 0.16 = 0.10$ . The resulting fractions of liquid and austenite just below the peritectic temperature are therefore given as:

$$\text{liquid} : g_l = 0.47 - 0.10 = 0.37 \quad \text{and} \quad \text{austenite} : g_\gamma = 1 - g_l = 0.63$$

The remaining liquid now transforms fully into austenite as the solid–liquid mixture cools down to the solidus temperature  $T_s = 1470^\circ\text{C}$ . This is referred to as the  $L + \gamma$  zone. (See [9] for an in-situ account of the solidification phase transformation of a peritectic steel). The freezing range  $\Delta T_f$  is given as:

$$\text{freezing range } \Delta T_f = T_l - T_s = 1515^\circ\text{C} - 1470^\circ\text{C} = 45^\circ\text{C}$$

It can be seen that hyperperitectic steels have longer freezing ranges compared to hypoperitectic steels, and high carbon steels ( $C > 0.53\%$ ) have even longer freezing ranges. In the latter, however, solidification starts with nucleation of FCC austenite instead of BCC  $\delta$ -ferrite.

Further cooling of the solidified steel down to  $800^\circ\text{C}$  results in the transformation of austenite into  $\alpha$ -ferrite (either allotriomorphic ferrite nucleating at the austenite grain boundaries or idiomorphic ferrite nucleating inside the austenite grains), until the eutectoid temperature of  $740^\circ\text{C}$  is reached. The remaining austenite in this hypoeutectoid steel then transforms into pearlite, a cooperative growth of  $\alpha$ -ferrite and cementite ( $\text{Fe}_3\text{C}$ ), hence showing up as a lamellae microstructure.

In the case of the 0.30% C steel, the volume fractions of  $\alpha$ -ferrite and pearlite ( $\alpha$ -ferrite + cementite) can similarly be determined using the lever rule:

$$\alpha\text{-ferrite} : g_\alpha = \frac{0.77 - 0.30}{0.77 - 0.02} = 0.63 \quad \text{and} \quad \text{pearlite} : g_{\text{pearlite}} = 1 - g_\alpha = 0.37$$

These volume fractions would be the case if no micro-porosity was present during the solidification stage, which is not exactly possible, even under highly efficient feeding of the mushy zone. Entrapped interdendritic liquid is bound to occur, even at high levels of solid fraction coherency. Porosity shows up as black (almost zero density) areas on a micrograph, which may sometimes be confused for the lower density phase ( $\alpha$ -ferrite), as shown on the micrographs in **Figure 8**.

Hence, it is important to establish the phase fractions as above, and use this data

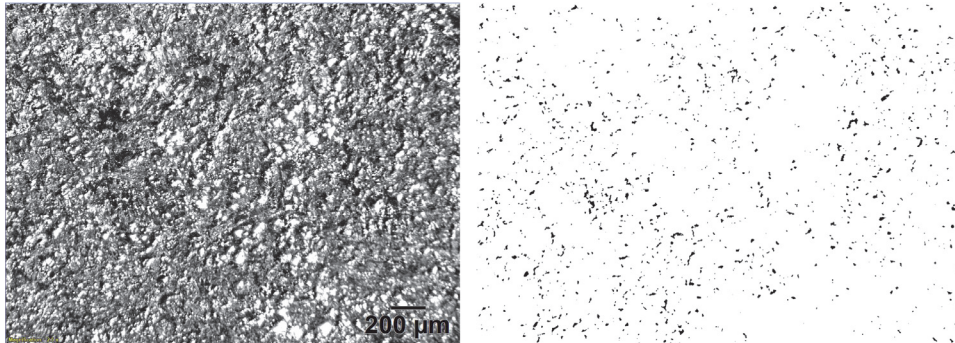


**Figure 8.** Optical Micrograph of an A216 WCB cast steel sample (left) and the contrasted image showing the porosity (right).



to distinguish between actual phases formed and porosity on a micrograph, since  $g_\alpha + g_{pearlite} + g_{pores} = 1$ . This effectively means that the density of the steel will be lower than its theoretical density, due to the formation of shrinkage pores.

The melt pouring temperature ( $T_p$ ) is often chosen without a clear understanding of its effect on macro and microstructural defects. Knowing the liquidus temperature ( $T_l$ ) allows a better choice of  $T_p$ . It is known that higher values of  $T_p$  increases the amount of porosity in castings [10], and increases hot tear susceptibility (HTS). The former is due to the increased possibility of hotspots, and the latter due to high thermally-induced stresses in the solidifying melt. Lower pouring temperatures are therefore preferred. **Figure 2** summarises the important temperature parameters during the solidification stage.

As a final word in this Section, the liquidus slope  $m$  and partition coefficient  $k$  can likewise be determined from the phase diagram of the steel alloy. An in-depth discussion on these parameters is beyond the scope of this Chapter, except to note that these parameters affect the spacing between secondary dendrite arms (as will be shown in Section 3.2), and hence the level of interdendritic shrinkage porosity. In peritectic steels, the liquidus slopes (temperature versus solute composition gradients) are given as  $m^\delta$  and  $m^\gamma$  for the  $L + \delta$  and  $L + \gamma$  zones respectively. Similarly, the partition coefficients for the solute in  $\delta$ -ferrite and austenite are given by:

$$k_C^\delta = \frac{C_{s,C}^*}{C_{l,C}^*} \quad \text{and} \quad k_C^\gamma = \frac{C_{s,C}^*}{C_{l,C}^*} \quad (7)$$

where  $C_{s,C}^*$  refers to the solute composition of carbon (subscript “C”) in the solid (subscript  $s$ ) within the multicomponent steel alloy, and  $C_{l,C}^*$  is similarly defined. The partition coefficient indicates the extent of solute rejection during the solidification process. Low values of  $k$  implies high levels of solute rejection. This can lead to high levels of microsegregation and, hence, inhomogeneity in microstructure – this is beyond the scope of this Chapter. As regards shrinkage porosity, the rejection of solute from the solidifying phase into the liquid melt contributes to the remelting of smaller dendrite arms and, subsequently, coarsening of larger dendrite arms. This is related to the difference in curvatures between the larger and smaller dendrite arms. A more detailed examination of dendritic coarsening can be found in [11]. The liquidus slopes and partition coefficients are important parameters for determining the evolution of solid fraction  $g_s$  as a function of temperature through the mushy zone, in the solution of shrinkage porosity formation, as will be shown in the next Section.

### 3.2 Mushy zone feeding

The nucleation and growth of the solid phase in the mushy zone involves highly complex phenomena, not all of which can be adequately dealt with in this Chapter. The aim here will be limited to discussing the mushy zone solidification in the context of shrinkage porosity formation. **Figure 9** depicts a typical equiaxed growth of a solid dendrite in a liquid melt, depicting the growth of secondary dendrite arms with spacing  $\lambda_2$ , and the velocity of the interdendritic feeding flow  $v_l$ . The velocity of the solidifying front is shown as  $v_T$ . The accompanying solidification contracts by a factor of:

$$\beta = (\rho_s - \rho_l) / \rho_l \quad (8)$$

(known as the solidification shrinkage factor), where  $\rho_s$  and  $\rho_l$  are the solid and liquid densities respectively. Hence, it can be shown that the (localised) feeding velocity becomes  $v_l = -\beta v_T$ .

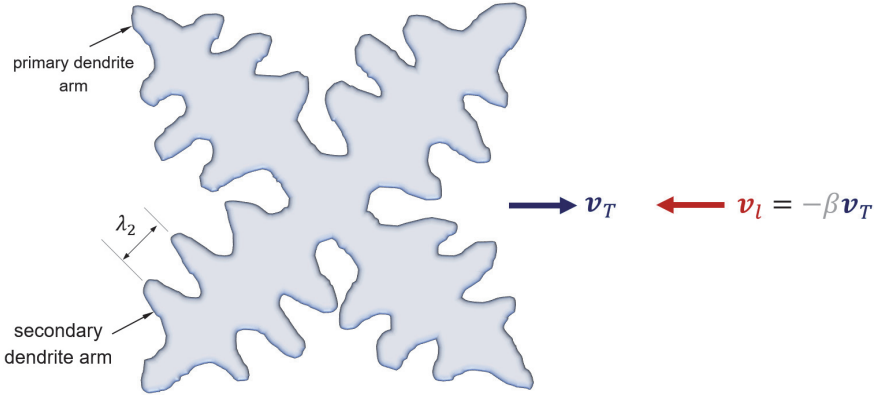


**Figure 9.**  
Dendritic growth in a liquid melt.

The densities of liquid steel (at  $T_l$ ) and solid steel (at  $T_s$ ) across the mushy zone freezing range depends on alloying composition and phase transformations. The metal's density increases as the temperature reduces from  $T_l$  to  $T_s$ , with further volumetric shrinkage to room temperature. Additionally, phase transformations (such as that at the eutectoid temperature from FCC austenite to  $\alpha$ -ferrite + cementite) change the degree of volumetric shrinkage. Refer to [12] for a more detailed discussion. The densities for different steel grades as a function of temperature can be determined using Thermo-Calc. In the case of A21 WCB steel, the value of  $\beta = 0.033$  was established in **Figure 1**.

As the mushy zone solidifies, the liquid fraction ( $g_l$ ) decreases at the expense of increasing liquid fraction ( $g_s$ ), assuming that no pore fraction ( $g_p$ ) forms ( $g_l + g_s + g_p = 1$ ) as shown in **Figure 10**. This means that, at any time, the average localised feeding velocity across the mushy zone becomes  $g_l v_l$ . This feeding velocity is dependent on the existence of a pressure gradient across the mushy zone, scaled by the permeability  $K$  of the mush zone and the dynamic viscosity of the liquid  $\mu$  – related by the well-known Darcy equation (derived from conservation of momentum in a porous medium):

$$g_l v_l = -\frac{K}{\mu} (\nabla p_l - \rho_l \mathbf{g}) \quad (9)$$

where  $p_l$  is the liquid pressure and  $\mathbf{g}$  is the gravitational acceleration.

The permeability of the porous mushy zone is modelled using the Kozeny-Carmen relation:

$$K(g_s(t_f), \lambda_2(t_f)) = \frac{\lambda_2^2(t_f) (1 - g_s(t_f))^3}{180 g_s^2(t_f)} \quad (10)$$

where  $\lambda_2$  is the secondary dendrite arm spacing (SDAS), dependent on the local solidification time  $t_f$  (the time for a point in the mushy zone to cool from the liquidus temperature  $T_l$  to the solidus temperature  $T_s$ ). Eq. (10) indicates that coarser grain structures (larger  $\lambda_2$ ) will increase the permeability  $K$ . Hence, coarser grain structure is preferred for higher permeability and improved feeding flow<sup>2</sup> [13]. In addition to

<sup>2</sup> It is noted that coarser grain structure can compromise the mechanical properties of a material, and it may be necessary to balance grain size for improved interdendritic flow and lower shrinkage porosity with mechanical properties, through controlling the solidification rate – see later.

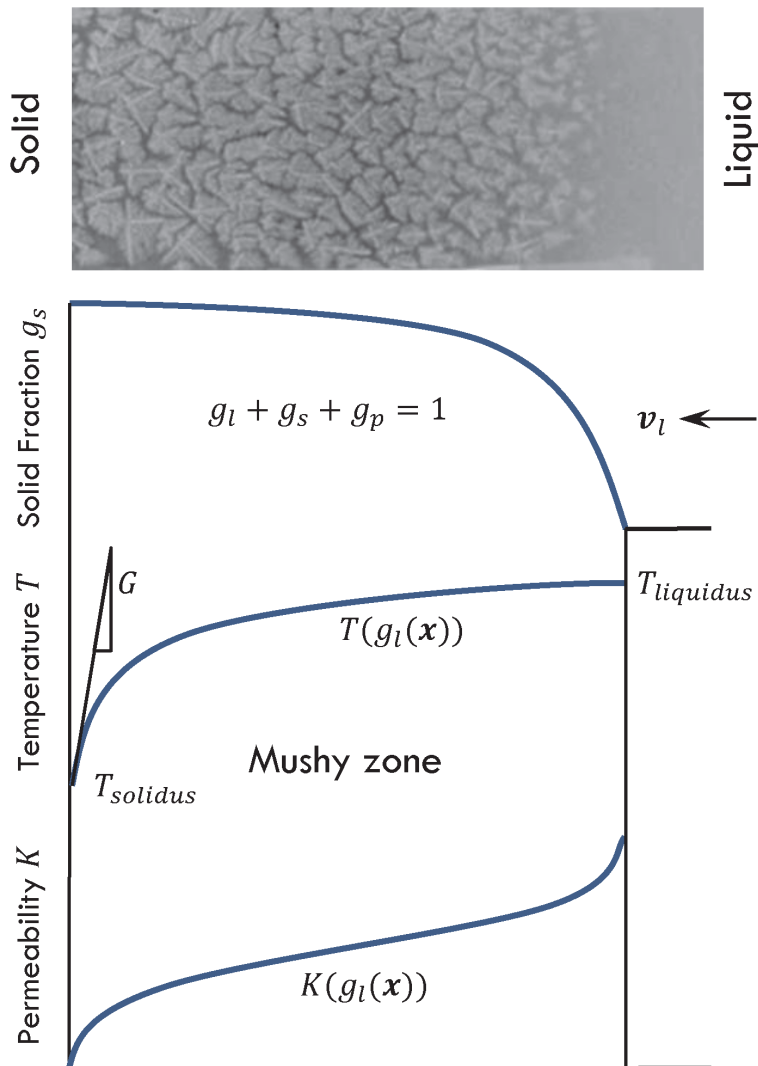


**Figure 10.** Two-dimensional view of a typical equiaxed mushy zone: solid fraction, permeability and temperature variation.

local solidification time, this *coarsening* process is further compounded by what is referred to as the *remelting* of adjacent smaller dendrite arms, due to phenomena related to curvature differences and solute diffusion. A detailed analysis can be found in [11], except to mention that the SDAS can be determined anywhere in the mushy zone using a coarsening law:

$$\lambda_2(t_f) = K_{t_f}(t_f)^{\frac{1}{3}} \quad (11)$$

where  $K_{t_f}$  is a coarsening parameter derived experimentally. More complex models, based on solute diffusion, solidification phase transformation and the Gibbs–Thomson coefficient for the material, can be found [11]. Perhaps a more practical approach is to write Eq. (11) in terms of cooling rate  $\dot{T}$  [14]:

$$\lambda_2(\dot{T}) = K_{\dot{T}}\dot{T}^{-\frac{1}{3}} \quad (12)$$

Ultimately, the interdendritic feeding velocity deep into the mushy zone drops rapidly (due to rapidly decreasing permeability), resulting in insufficient feeding flow and, hence, the onset of shrinkage porosity. Applying the conservation of mass ( $\partial\rho/\partial t + \nabla \cdot (\rho\mathbf{v}) = 0$ ) to the liquid domain:

$$\frac{\partial}{\partial t} (\rho_s g_s + \rho_l g_l) + \nabla \cdot (\rho_l g_l \mathbf{v}_l) = 0 \quad (13)$$

and substituting the Darcy Eq. (9), assuming that the gravitational pressure head in a sandcast is the actual pressure gradient, gives:

$$\underbrace{(\rho_s - \rho_l) \frac{\partial g_s}{\partial t} + \frac{\partial \rho_l}{\partial t} (1 - g_s - g_p)}_{\text{pore information}} + g_s \underbrace{\left( \frac{\partial \rho_s}{\partial t} - \rho_l \frac{\partial g_p}{\partial t} \right)}_{\text{solidification shrinkage}} = \nabla \cdot \underbrace{\left( \rho_l \frac{K}{\mu} (\nabla P_l) \right)}_{\text{feeding}} \quad (14)$$

where  $g_l + g_s + g_p = 1$  has been used to introduce the pore fraction in place of the liquid fraction. This form of the conservation equations gives a sense of the terms responsible for capturing (a) the shrinkage porosity compensated by feeding flow (positive) and (b) the pore formation due to a lack of feeding flow (negative). Eq. (14) can be reformulated by introducing the Kozeny-Carmen relation (Eq. (10)) and assuming that the liquid and solid densities variations ( $\partial\rho_l/\partial t$  and  $\partial\rho_s/\partial t$ ) are minimal across the freezing temperature range:

$$(\rho_s - \rho_l) \frac{\partial g_s}{\partial t} - \rho_l \frac{\partial g_p}{\partial t} = \nabla \cdot \left( \rho_l \frac{1 K_T^2 \dot{T}^{-\frac{2}{3}} (1 - g_s)^3}{\mu 180 g_s^2} (\nabla P_l) \right)$$

and introducing  $\beta$  from Eq. (8), a concise mathematical form for shrinkage pore formation in the mushy zone can be established:

$$\beta \frac{\partial g_s}{\partial t} - \frac{\partial g_p}{\partial t} = \nabla \cdot \left( \frac{1 K_T^2 \dot{T}^{-\frac{2}{3}} (1 - g_s)^3}{\mu 180 g_s^2} (\nabla P_l) \right) \quad (15)$$

In practice, though, shrinkage porosity prediction is often based on a quantitative criterion, based on the scaling of the pressure gradient given in Eq. (15). By substituting for solid fraction  $g_s$  as a function of temperature (see **Figure 10**), using a microsegregation model (such as the lever rule or the Gulliver-Scheil model), it is possible to integrate Eq. (15) to obtain such a scaling parameter, and use this as a *criterion* for shrinkage pore formation. The scaling parameter, known as the Niyama criterion, given by:

$$N_y = \frac{G}{\sqrt{\dot{T}}} \quad (16)$$

where  $G$  is the temperature gradient at the solid-melt interface and  $\dot{T}$  is the cooling rate, is currently the most widely used criterion for porosity prediction in metal casting. Niyama et al. [15] initially used this criterion to study porosity formation in steel castings, and concluded that (macro) porosity occurs when  $N_y < 1$ , i.e. low temperature gradient  $G$  and/or high cooling rate  $\dot{T}$ . Carlson and Beckermann [16] investigated the use of the Niyama criterion for shrinkage porosity in nickel alloy castings by simulating the filling and solidification and correlating the Niyama criterion with (micro- and macro-) porosity-containing areas in the

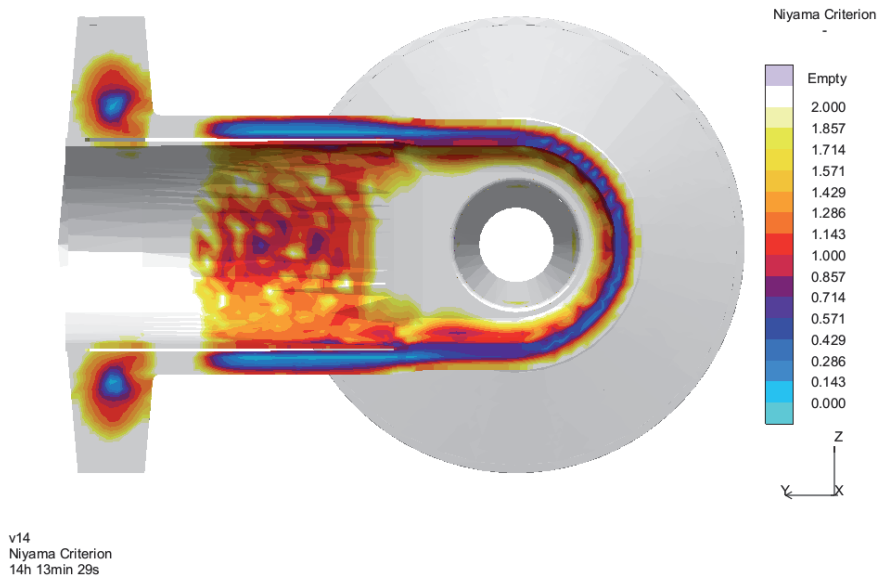


**Figure 11.** Distribution of Niyama criterion values for a steel casting, showing macroporosity ( $N_y < 1$ ) and microporosity ( $N_y < 1$ ) in critical areas.

actual castings. They found that macroporosity (visible on radiographs) correlated to values of Niyama criterion  $N_y < 1$ , but also found that microporosity occurs at higher values of Niyama criterion  $N_y < 2$  for nickel based alloys. Hence, critical areas in a steel casting should have values of Niyama criterion of at least  $N_y > 2$  to be a sound casting (**Figure 11**).

Although the Niyama criterion, and other similar thermal criteria, such as that proposed by Lee et al [17] and Suri et al [18], are only quantitative indicators, it allows process control interventions to reduce shrinkage porosity formation. From the Niyama criterion (Eq. 16), it is clear that reducing the cooling rate ( $\dot{T}$ ) will result in higher values of  $N_y$  and, hence, lower levels of shrinkage porosity - as mentioned before, this is due to coarser grain structures with higher permeability (i.e. improved feeding flow). Practically, this may involve preheating the mould, or/and using silica sand with lower thermal conductivity.

Furthermore, high thermal gradients ( $G$ ), will also lead to higher values of  $N_y$ . From **Figure 10**, it is clear that lower freezing range allows (i.e. narrower mushy zones) will provide higher values of  $G$ , resulting in more columnar dendritic growth with higher permeability, as opposed to equiaxed growth with lower permeability.

#### 4. Classification of Shrinkage Porosity Types

In the previous sections, the mechanisms for shrinkage porosity formation were discussed, from a thermal perspective – that is, during solidification contraction of the mushy zone. In this section, the various types of shrinkage porosity, based on morphology, will be classified. In doing so,, it is important to understand their likely causes, at least from a foundry perspective. A useful approach is to look at these causes in terms of design (both part and mould design), process and material factors.

At the outset, it is important to distinguish between micro and macro shrinkage porosity. A common misconception is to make this distinction purely based on

length scale, for which there are different interpretations of what constitutes a micro or macro pore. A more substantive approach is to base this distinction on the microstructural and macrostructural phenomena involved.

**Shrinkage Macro-Porosity.** Part and mould geometry are largely responsible for shrinkage macro-porosity formation. Sudden increases in geometric volume can lead to the formation of hotspots, or entrapped liquid melt that solidifies inward (as was demonstrated in **Figure 5**). In such cases, the morphology can range from large spherical pores to large linear cracks (**Figure 12**), the latter also referred to as cold cracks.

Hotspots are large (macro) regions of entrapped liquid, surrounded by a frozen skin layer. Such regions initially lead to surface sinks until the frozen skin layer develops sufficient resistance to deformation, giving rise to large internal shrinkage pores. In cases where the hotspot is partially exposed to low-pressure liquid feeding, such as close to a gate, the porosity takes on either a layered morphology, referred to as layered shrinkage porosity (see **Figure 13**), or a pipe morphology, referred to as pipe shrinkage porosity.

Hot tears, as opposed to hotspot-induced shrinkage porosity, occur as a result of deformation caused by thermally-induced stresses. The volume fraction at which the mushy zone develops resistance to deformation, due to the coalescence of dendrite arms (see **Figure 10**), is referred to as the coherency point. The solid

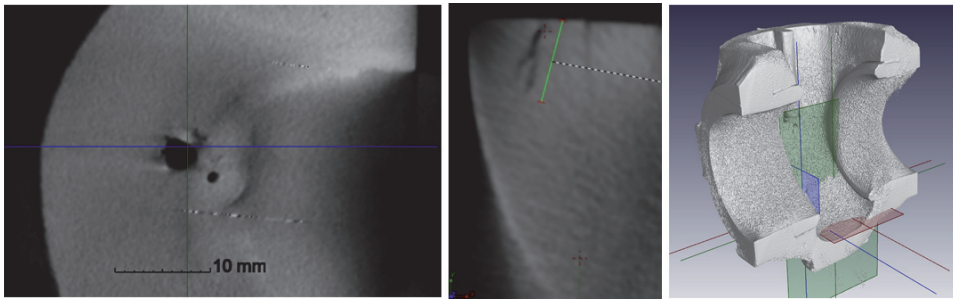


**Figure 12.** Formation of macro shrinkage pores due to hotspot (left) and hot tearing / cold cracking (centre) located using computed tomography (CT) scanning (right).

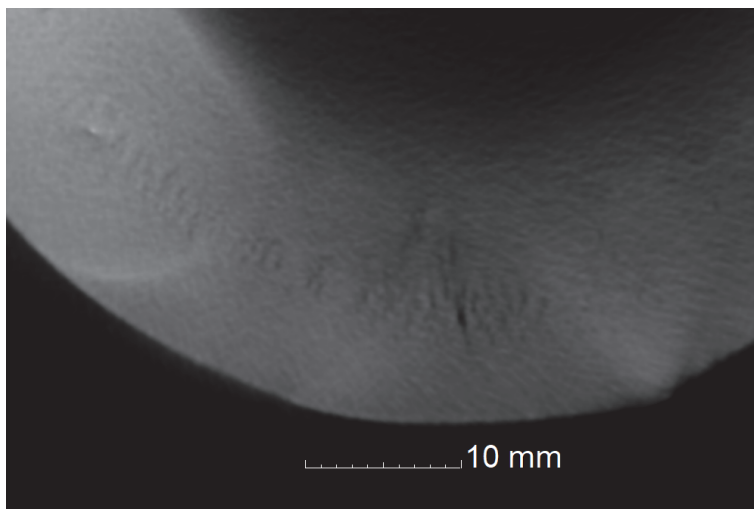


**Figure 13.** Formation of layered macro shrinkage porosity due to a hotspot partially exposed liquid feeding.

fraction at which this occurs depends on factors such as solidification rate  $\dot{T}$ , the alloy freezing range and the diffusion of solute, and is typically in the region of  $g_s = 0.8$  to  $g_s = 0.95$  [11, 19]. At this point in the evolution of solid fraction, resisting stresses develop. Coupled with low permeability (i.e. lack of feeding), especially in low-freezing range alloys in which coarser dendritic structures evolve, solidification contraction of intergranular liquid can result in hot tearing. Although hot tearing is a microstructural phenomenon [20], it shows up as large intergranular cracks at the macrostructural scale.

Improving the pressurisation of the mould, through a combination of part geometry modifications and feeder design, can reduce or even eliminate the occurrence of hotspots, hot tears and layered porosity. In many cases, part design is often overlooked – this includes reducing sudden expansions in part volume, and introducing tapered flow regions in the part [21, 22] to improve feeding flow.

**Shrinkage Micro-Porosity.** As opposed to shrinkage macro-porosity, which is due to macrostructural effects such as hot spots and skin-freezing, micro-porosity is due to interdendritic shrinkage of entrapped liquid melt, nucleating mostly between secondary dendrite arms. As discussed in Section 3, the SDAS depends on the cooling rate during solidification, as well as the freezing range [14], the latter influenced by the carbon content of the steel [6], or, in general, chemical compositions of the major alloying elements. Depending on these factors, the SDAS can vary from as low as 50  $\mu\text{m}$  to as high as 700  $\mu\text{m}$  [7], thus influencing the size of shrinkage micro-pores. For example, for a low carbon steel of 0.19%wt C, the size of the SDAS was found to be in the range of 67–311  $\mu\text{m}$ , for cooling rates varying from 10 to 0.1°C/s [13].

Hence, the length scales of shrinkage micro-porosity may be as low as a few microns, increasing to multiple values of the SDAS in the case of interconnected interdendritic melt. Furthermore, three different pore morphologies can occur: linear, feathery and sponge, depending largely on the freezing range of the alloy and the cooling rate, as previously discussed. The different morphologies present different challenges with regards to part quality, with linear micro-porosity being classified as more severe as compared to sponge micro-porosity (as will be discussed further in the next section). Whilst the choice of alloy in many cases is out of the control of the foundry (and depends on client specifications based), understanding the mechanisms for shrinkage micro-porosity in terms of alloy freezing range is important in assessing expected part quality. Foundries can, though, control the cooling rate of the casting for a desired microstructure.

Importantly, the casting process parameters that prevail during the solidification phase have a direct impact on mechanical properties, such as strength and ductility (as a result of grain size), as well as microsegregation, although the latter could be remedied through solution heat treatment. For example, lower solidification rates lead to coarser microstructure (i.e. larger grain size), and hence improved interdendritic feeding. This can also improve material homogeneity (due to back-diffusion of solute); however, it will result in reduced ductility of the material (due to the coarser grain structure). Hence, the optimisation of casting and process parameters for reducing shrinkage porosity may need to be balanced with desired microstructural qualities, leading to multiple (and often conflicting) objectives during the optimisation process [10].

Shrinkage micro-porosity may present itself as three different distinct morphologies: Linear, Feathery and Sponge. The causes of these different morphologies are noted as follows:

- The morphology of shrinkage micro-porosity depends on the freezing range (a function of alloy composition), and solidification rate. The latter influences the



**Figure 14.**  
*Morphologies of linear (left) and feathery (right) shrinkage porosity.*

permeability of the interdendritic region, in terms of SDAS, solid fraction distribution and point of coherency.

- In long-freezing-range alloys, due to inefficient liquid feeding of the interdendritic regions (as a result of pressure drops in the high-solid fraction region of the mushy zone), the resulting effect is that of a partially drained sponge, and hence the term “sponge porosity” for this defect (see **Figure 8**).
- In short freezing range alloys, the smoother solidification fronts lead to linear shrinkage defects, often of a feathery morphology. With low solidification rates, due to larger dendrite sizes and ensuing coarsening/remelting of neighbouring dendrite arms. A linear morphology prevails – **Figure 14**.

## 5. Porosity inspection

Procedures for porosity inspection in castings are specified under the relevant industry standard, depending on the material, thickness of the casting and the radiographic technique used. These procedures, based on the ASTM standards, are listed in **Table 2** for different part thicknesses.

In this Chapter, reference will be limited to the ASTM E2868 standard (Standard Digital Reference Radiographs for Steel Castings Up to 2 inches (50.8 mm) in Thickness). This is the equivalent of ASTM E446 for film radiography, both of which are similar to their heavy-walled counterparts. The approach developed here can therefore be applied to any of these standards. The ASTM E2868 standard provides a set of five digital reference radiographic images (nominal 250 kV X-rays) for each type of shrinkage porosity (CA - linear, CB – feathery, CC – sponge, CD – combined) from the lowest severity level 1 to the highest severity level 5 (as shown in **Figure 15** for the case of sponge shrinkage porosity), for comparison with production radiographs. The reference radiographs can be generated for a comparable resolution (pixel size) to that of the production radiographs.

	Thin-walled	Heavy-walled	Heavy-walled
Standard (film) reference radiographs	ASTM E446	ASTM E186	ASTM E280
Standard digital reference radiographs	ASTM E2868	ASTM E3030	

**Table 2.**  
*ASTM standards for film and digital radiography of steel castings.*



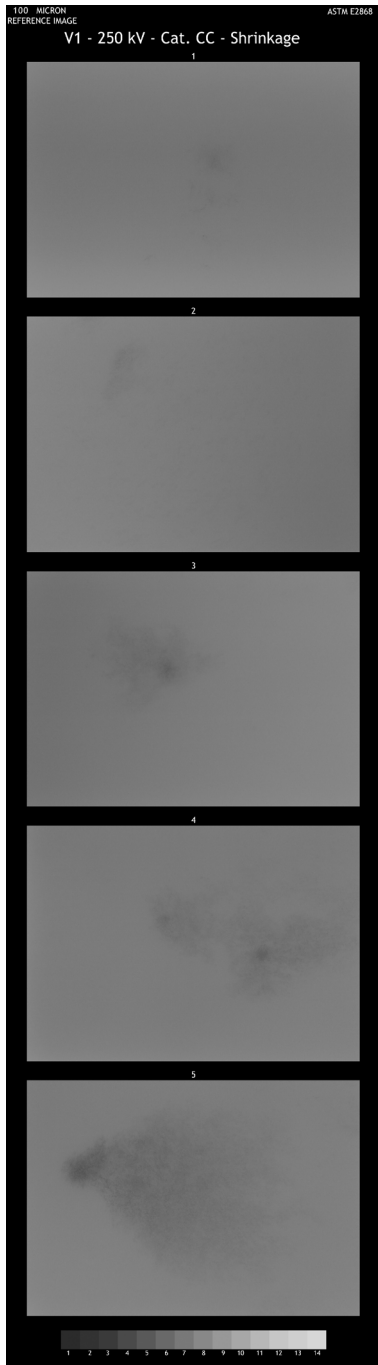


**Figure 15.** Original (left) and contrasted (right) 100  $\mu\text{m}$  resolution ASTM E2868 digital reference radiographs for shrinkage porosity Category CC (sponge), severity levels 1–5.

Production radiographs are commonly obtained using conventional X-ray techniques. Lately, X-ray Computed Tomography (CT) is gaining popularity for internal defect identification [23]. Reasons include the ability to determine pore morphologies in 3D, and resolutions as low as 1  $\mu\text{m}$  (voxel size) suitable for micro-porosity detection. For comparison with reference radiographs as per the industry

standards, 3D CT scans can be collapsed into equivalent 2D images, using a “thick slab” feature of CT scanning image analysis software [24].

The standard digital reference radiographs provide resolutions as low as 20  $\mu\text{m}$  (pixel or voxel size) – however, it may not be possible to generate such high resolution production radiographs in practice due to equipment limitations, especially in the case of high density materials such as steels. Hence, a 100  $\mu\text{m}$  resolution is seen as adequate for detection within the typical SDAS length scale (for ferrous metals).

Allowable porosity levels are often based on client specifications, but may also be part of quality standards associated with particular components. Such acceptance criteria, as in the case of high-performance valves for example, are shown in **Figure 16**.

The inspection process requires the area of the production radiograph to be prorated to an area of interest of the reference radiograph, as illustrated in **Figure 17**, and visually compared to establish the matching severity level.

Shrinkage Porosity Type	Category	Acceptable comparative radiograph (ASTM E446 / ASTM E2868)
Shrinkage - linear	CA	CA2
Shrinkage - feathery	CB	CB3
Shrinkage - sponge	CC	CC3
Shrinkage - combined	CD	CD3

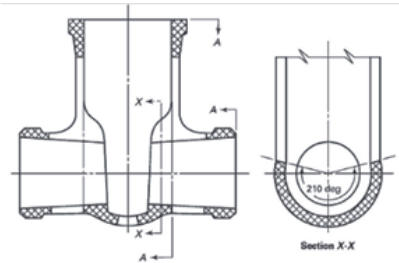


**Figure 16.**

Acceptance criteria for shrinkage porosity in steel valve castings of wall thickness  $\leq 50.8$  mm (ASME B16.34), showing the critical regions on the right.

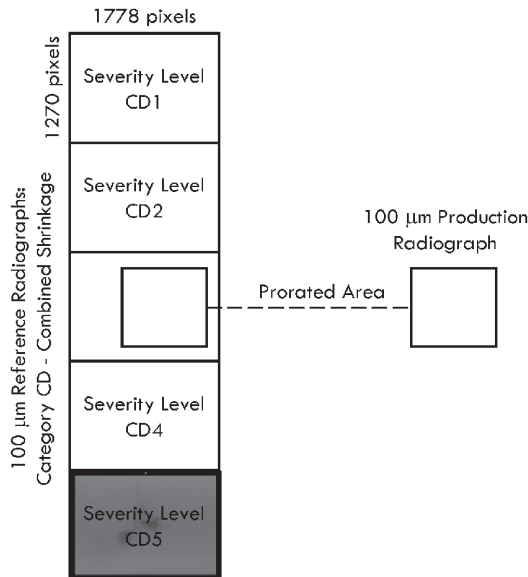


**Figure 17.**

Evaluating the porosity severity level by comparing the production radiograph with the reference radiographs of comparable resolution (e.g. 100  $\mu\text{m}$  = 10 pixels/mm) from ASTM E2868, for a particular category of shrinkage porosity (e.g. CD - combined shrinkage porosity).

This inspection process is considered to be subjective, and other objective methods based on image processing have been suggested [25, 26], a subject for further development in the future.

## 6. Summary

An overview of shrinkage porosity is given, with reference to steel sand castings, from investigating the causes of shrinkage porosity to possible mitigation approaches, and finally the importance of understanding the technologies associated with the inspection and evaluation of shrinkage porosity severity levels. Further analysis of certain aspects of shrinkage porosity may be undertaken where an in-depth understanding is required. In summary, the following points are noted:

1. Shrinkage micro-porosity arises during the solidification contraction of an alloy. Hence, the steel's phase transition and density properties in the mushy zone are important in understanding the likely mechanisms and expected morphologies of shrinkage porosity.
2. Linked to this, the lack of interdendritic feeding of the mushy zone as its solid fraction increases beyond a certain point, referred to as the coherency point, leads to interdendritic pore nucleation. In large freezing range alloys, the result is a sponge morphology, migrating to feathery linear morphologies as the freezing range decreases (with decreasing carbon content).
3. However, the cooling rate is a determining factor for secondary dendrite arm spacing, and hence level of shrinkage porosity in an alloy. This gives the foundry a degree of control in avoiding the more severe linear porosity.
4. At the intergranular level, entrapped liquid melt can lead to hot tearing, due to the weak resisting forces of the coherent dendritic structure, succumbing to inward pressure. Hence, hot tearing may show up as macro-porosity in castings.
5. Shrinkage macro-porosity, on the other hand, is due to large entrapped liquid volume that cannot be adequately fed by the feeder system because of skin freezing. Whilst hotspots can easily be overcome through part and mould design modifications, narrow long sections may experience layered porosity due to declining pressurization of the mould as the skin layer thickens. Special attention should therefore be given to the design of the feeder system in such castings. This also goes for hotspots in the junction region between the casting and a feeder, which can lead to pipe shrinkage porosity extending into the part.
6. It was shown that certain thermal criteria may be used in practice in determining or reducing the level of shrinkage porosity, both micro-porosity and macro-porosity.
7. Finally, assessing the severity level of porosity in a casting is necessary in determining the acceptability of cast part quality. A range of standards have been issued, which provide the foundry with a benchmark in terms of acceptance criteria for the various types of shrinkage porosity.

## **Acknowledgements**

The author wishes to thank Llewellyn Cupido for producing some of the figures and for generating the Thermo-Calc data used in the Chapter.


## **Author details**

Nawaz Mahomed  
Stellenbosch University, Stellenbosch, South Africa

\*Address all correspondence to: [nawaz@sun.ac.za](mailto:nawaz@sun.ac.za)

## **IntechOpen**

---

© 2020 The Author(s). Licensee IntechOpen. This chapter is distributed under the terms of the Creative Commons Attribution License (<http://creativecommons.org/licenses/by/3.0>), which permits unrestricted use, distribution, and reproduction in any medium, provided the original work is properly cited. 

## References

- [1] Hardin RA, Beckermann C. Effect of Porosity on the Stiffness of Cast Steel. *Metall Mater Trans A*. 2007;**8**(12): 2992-3006. DOI: 10.1007/s11661-007-9390-4
- [2] Ol'khovik E. Study of the Effect of Shrinkage Porosity on Strength of Low Carbon Cast Steel. *IOP Conf Ser-Mat Sci*. 2015;**91**(1). ISSN 1757-8981
- [3] Sigl K., Hardin R.A., Stephens R., Beckermann C. Fatigue of 8630 cast steel in the presence of porosity. *Int J Cast Metal Res*. 2004;**17**(3):130-146. DOI: 10.1179/136404604225020588
- [4] Campbell J. *Castings*. 2nd ed. Oxford: Butterworth-Heinemann; 2003. 335 p. ISBN: 0750647906
- [5] Jimbo, I., Cramb, A.W. The density of liquid iron-carbon alloys. *Metall Mater Trans B*. 1993;**24B**: 5-10. DOI: 10.1007/BF02657866
- [6] Pierer R., Barnard C. On the influence of carbon on secondary dendrite arm spacing in steel. *J. Mater. Sci*. 2008;**43**:6938-6943. DOI 10.1007/s10853-008-2985-3
- [7] El-Bealy M., Thomas B.G. Prediction of Dendrite Arm Spacing for Low Alloy Steel Casting Processes. *Metall Mater Trans B*. 1996;**27B**: 689-692. 10.1007/BF02915668
- [8] Martinik O. *et al.* Experimental and Theoretical Assessment of Liquidus, Peritectic Transformation, and Solidus Temperatures of Laboratory and Commercial Steel Grades. *Journal of Phase Equilibria and Diffusion*. 2019;**40**(1):93-103. DOI: 10.1007/s11669-019-00707-1
- [9] Chen H. *et al.* Phase Transition of Peritectic Steel Q345 and Its Effect on the Equilibrium Partition Coefficients of Solutes. *Metals*. 2017;**7**(8):Article 288. DOI: 10.3390/met7080288
- [10] Mahomed N., Kleynhans H.A. Reducing Shrinkage Porosity in High-Performance Steel Castings: Case of an ASME B16.34 Gate Valve Body: Part 2 — Simulation and Experimental Verification. *Int J Metalcast*. 2019;**13**(2): 463-472. DOI: 10.1007/s40962-018-0275-7
- [11] Dantzig J.A., Rappaz M. *Solidification*. 1<sup>st</sup> ed. Lausanne: EPFL Press; 2009. 621 p. ISBN:978-2-940222-17-9
- [12] Tesfaye Firdu F., Taskinen P. Densities of Molten and Solid Alloys of (Fe, Cu, Ni, Co) - S at Elevated Temperatures - Literature Review and Analysis. *Aalto University Publications in Materials Science and Engineering*, Espoo; 2010.
- [13] Carlson K.D., Beckermann C. Prediction of Shrinkage Pore Volume Fraction Using Dimensionless Niyama Criterion. *Metall Mater Trans A*. 2009;**40**:163-175. DOI: 10.1007/s11661-008-9715-y
- [14] Zhao J., Yan P. The Effect of Cooling Rate of Solidification on Microstructure and Alloy Element Segregation of As Cast Alloy 718. In: *Proceedings of the International Symposium on Superalloys and Various Derivatives*; 17 June 2001; Pittsburgh. P. 133-140
- [15] Niyama E., Uchida T., Morikawa M., Saito S. A Method of Shrinkage Prediction and its Application to Steel Casting Practice. *Int. Cast. Met. J*. 1982;**7**(3): 52-63.
- [16] Carlson K.D., Beckermann C. Use of the Niyama Criterion to Predict Shrinkage-related Leaks in High-Nickel Steel and Nickel-Based Alloy Castings. In: *Proceedings of 62nd SFSA Technical and Operating Conference*. 2008; Chicago. Steel Founders Society of America. Paper No. 5.6

- [17] Lee Y. W., Chang E., Chieu C. F. Modeling of feeding behavior of solidifying Al-7Si-0.3Mg alloy plate casting. *Metall. Mater. Trans. B.* 1990;21(4):715–722. DOI: 10.1007/BF02654250
- [18] Suri V.K., Paul A.J., El-Kaddah N., Berry J.T. Determination of correlation factors for prediction of shrinkage in castings, Part I: Prediction of microporosity in castings: a generalised approach. *AFS Trans.* 138, 861–867, 1994
- [19] Khalajzadeh V., Beckermann C. Simulation of Shrinkage Porosity Formation During Alloy Solidification. *Metall Mater Trans A.* 2020;51A:2239–2254. DOI: 10.1007/s11661-020-05699-z
- [20] Ridolfi M.R. Hot Tearing Modeling: A Microstructural Approach Applied to Steel Solidification. *Metall Mater Trans B.* 2014;45B:1425–1438. DOI: 10.1007/s11663-014-0068-1
- [21] Riedler M., Michelic S., Bernhard C. Formation of shrinkage porosity during solidification of steel: Numerical simulation and experimental validation. *IOP Conf Ser-Mat Sci.* 2016;143(1). DOI:10.1088/1757-899X/143/1/012035
- [22] Monroe C.A., Gorsky D.A., Huff R. K., Grandhi R.V. Improving the Directional Solidification of Complex Geometries through Taper Addition. *Int. J. Metalcast.* 2014;8(3):23–27. DOI: 10.1007/BF03355587
- [23] Yang Z., Kang J., Wilkinson D.S. Characterization of Pore Defects and Fatigue Cracks in Die Cast AM60 Using 3D X-ray Computed Tomography. *Metallurgical and Materials Transactions B.* 2015;46B:1577–1585. DOI: 10.1007/s11663-015-0370-6
- [24] Mahomed N., Kleynhans H.A. Reducing Shrinkage Porosity in High-Performance Steel Castings: Case of an ASME B16.34 Gate Valve Body: Part 1 — Analysis, Techniques and Experimental Approach. *Int J Metalcast.* 2018;12(4): 919–926. DOI: 10.1007/s40962-018-0226-3
- [25] Carlson K., Ou S., Hardin R., Beckermann C. Analysis of ASTM X-ray shrinkage rating for steel castings. *Int. J. Cast Metals Res.* 2001;14:169–183. DOI: 10.1080/13640461.2001.11819436
- [26] Blair M., Monroe R., Hardin R., Beckerman C., A New Standard for Radiographic Acceptance Criteria for Steel Castings. In: *Proceedings of the 62nd SFSA Technical and Operating Conference; 2008; Chicago. Steel Founders' Society of America. Paper No. 5.5*